

Fluctuations in an Equilibrium Convective Ensemble. Part II: Numerical Experiments

BRENDA G. COHEN

Department of Meteorology, University of Reading, Reading, United Kingdom

GEORGE C. CRAIG

DLR Institut für Physik der Atmosphäre, Oberpfaffenhofen, Germany

(Manuscript received 22 March 2005, in final form 14 October 2005)

ABSTRACT

The theoretical predictions derived in Part I of this study for the equilibrium fluctuations of an idealized ensemble of noninteracting, pointlike cumulus clouds are tested against three-dimensional cloud resolving model (CRM) simulations of radiative–convective equilibrium. Simulations with different radiative cooling rates are used to give a range of cloud densities, while imposed vertical wind shear of different strengths is used to produce different degrees of convective organization. The distribution of mass flux of individual clouds is found to be exponential in all simulations, in agreement with the theory. The distribution of total mass flux over a finite region also agrees well (to within around 10%) with the theoretical prediction for all simulations, but only after a correction to the modeled variance to take account of the finite size of clouds has been made. In the absence of imposed vertical wind shear, some spatial clustering of convective cells is observed at lower forcings (-2 and -4 K day $^{-1}$) on a scale of 10–20 km, while at higher forcings (-8 , -12 , and -16 K day $^{-1}$), there is a tendency toward spatial regularity on the same scale. These localized cloud interactions, however, appear to have little effect on the magnitude of the mass flux variability. Surprisingly, the convective organization obtained in the simulations with vertical wind shear has only a small effect on the mass flux statistics, even though it shows clearly in the location of the clouds.

1. Introduction

In Craig and Cohen (2006, hereafter Part I) of this investigation, theoretical predictions for the fluctuations of an ensemble of noninteracting, pointlike convective clouds in equilibrium with the large-scale forcing are obtained through an elementary application of the Gibbs canonical ensemble. In this method, the statistical properties of the fluctuations are predicted to follow the most probable distribution subject to certain external constraints. In particular, if the ensemble mean mass flux in a given region at a given height is $\langle M \rangle$, and it is distributed randomly among individual clouds such that the mean mass flux per cloud is $\langle m \rangle$, then the mean number of clouds in the region is $\langle N \rangle$, and an exponential distribution of individual cloud mass fluxes (analogous to the Boltzmann distribution of molecular energies) is expected; that is,

$$d\bar{n}(m) = \frac{\langle N \rangle}{\langle m \rangle} e^{-m/\langle m \rangle} dm, \quad (1)$$

where $d\bar{n}(m)$ is the average number of clouds in the ensemble possessing a mass flux between m and $m + dm$.

Ignoring cloud interactions leads to the expectation that the number of clouds within the given region will be random, and if the clouds are assumed to be pointlike, it will be described by a Poisson distribution:

$$p_N(n) = \frac{\langle N \rangle^n e^{-\langle N \rangle}}{n!} \quad \text{for } n = 0, 1, \dots \quad (2)$$

This relation, together with the exponential distribution of cloud mass fluxes, can be used to derive a theoretical expression for the distribution of total mass flux in the ensemble, $p(M)$:

$$p(M) = \left(\frac{\langle N \rangle}{\langle m \rangle} \right)^{1/2} e^{-\langle N \rangle} M^{-1/2} e^{-M/\langle m \rangle} I_1 \left(2 \sqrt{\frac{\langle N \rangle}{\langle m \rangle}} M \right), \quad (3)$$

Corresponding author address: George C. Craig, DLR Oberpfaffenhofen, Institut für Physik der Atmosphäre, Münchner Strasse 20, D-82234 Wessling, Germany.
E-mail: george.craig@dlr.de

where M is the total mass flux of the system, and $I_1(x)$ is the modified Bessel function of order 1.

Finally, the normalized variance of the total mass flux distribution can be derived, and is of the form

$$\frac{\langle(\delta M)^2\rangle}{\langle M\rangle^2} = \frac{2}{\langle N\rangle}. \quad (4)$$

As mentioned in Part I, moist atmospheric convection does not formally satisfy the noninteracting and point-particle assumptions used in the derivation of the above relations. This idealized approach, however, may become approximately valid in the limit of low cloud number density (where cloud interactions become negligible) and regions large compared to the area occupied by individual clouds (where the finite size of clouds becomes unimportant). In this paper, the applicability of the statistical theory to convective systems within the range of atmospheric interest is assessed by comparing the theoretical predictions of Eqs. (1), (3), and (4) against cloud mass flux data obtained from a three-dimensional (3D) cloud resolving model (CRM), in a state of radiative–convective equilibrium. A series of simulations will be considered. The first case will be with weak forcing and no environmental vertical wind shear, leading to isolated unorganized convective cells. This is the case where the assumptions are most likely to be satisfied. Further simulations will have stronger forcing, leading to more closely spaced cells, and will introduce vertical wind shear of two different magnitudes, giving differing degrees of convective organization.

2. Model formulation and setup

A CRM should be an appropriate choice of numerical tool for this investigation, since it can explicitly resolve cloud-scale dynamics, although the resolution used in this study is too coarse to describe structures within the clouds. The Met Office large-eddy model (LEM) used here is summarized briefly in the following section, and is described in more detail by Shutts and Gray (1994) and Tompkins and Craig (1998). The details of the setup of the numerical experiments are given in section 2b.

a. Model formulation

The dynamical core of the CRM solves the anelastic, Boussinesq approximation to the prognostic momentum and thermodynamic equations, given in Shutts and Gray (1994). Liquid water temperature is used as the prognostic thermodynamic variable, since it is reasonably accurately conserved in deep moist ascent (Shutts

1991). The advection scheme is the total variation diminishing (TVD) scheme of Leonard (1991), which is capable of advecting sharp gradients without overshoots.

Parameterization of subgrid scale turbulence is accomplished using a first-order Smagorinsky–Lilly closure (Mason 1989), modified to include a dependence on the pointwise moist Richardson number (MacVean and Mason 1990). Surface fluxes are parameterized using similarity theory. The microphysical parameterization used is the three-phase ice scheme of Swann (1994) and Brown and Swann (1997), with prognostic equations for six microphysical variables: mass mixing ratios of liquid cloud water, rain drops, ice crystals, snow crystals, graupel and also the number concentration of ice crystals.

The domain size used is $128 \times 128 \times 21 \text{ km}^3$, with horizontal resolution of 2 km and a stretched grid in the vertical (100 m in boundary layer, 500 m in upper troposphere). For the organized convection simulations described in section 5, a larger domain of $256 \times 256 \text{ km}^2$ is employed. A Newtonian damping layer is applied over a layer of 3 km, from a height of 16.75 km, with a damping coefficient of 0.001 s^{-1} . The lateral boundary conditions are bi-periodic, which is appropriate for simulation of a homogeneously forced flow.

b. Design of the numerical experiments

The CRM is set up to simulate a region of the tropical atmosphere in radiative–convective equilibrium. The radiative forcing is provided via a constant, horizontally homogeneous cooling rate, imposed up to a height of 400 mb, then decreasing linearly to 0 between 400 and 200 mb. The lower boundary represents an ocean surface with a fixed, uniform sea surface temperature of 300 K. The atmosphere is assumed to be nonrotating, and in the first set of simulations no mean wind is imposed. This setup is almost identical to that of Robe and Emanuel (1996). By deliberately omitting processes such as cloud–radiative interactions, wind shear, and background rotation that are known to cause convective organization (see, e.g., Tompkins and Craig 1998; Thorpe et al. 1982; Vallis et al. 1997), the intention is to generate an idealized equilibrium convective ensemble most suited to comparison with the statistical theory derived in Part I. The model is run into a full radiative–convective equilibrium state (reached after 10–20 days of simulation, depending on forcing), and the variability of the convective ensemble within this equilibrium period is compared with theory.

Space–time averages over the full horizontal extent of the domain at a height of 2.4 km (corresponding to the top of the shallow convection layer and coinciding

with a minimum in mean moist static energy), and over a period of several hours within the equilibrium state, are used to approximate the theoretical ensemble average quantities in Eqs. (1), (3), and (4). Similar results have also been obtained using a reference height of 1 km, just above the cloud-base level. Five different equilibrium states are simulated, with cooling rates of -2 , -4 , -8 , -12 , and -16 K day $^{-1}$. A cooling rate of -2 K day $^{-1}$ represents the typical net cooling over the tropical oceans (Sui et al. 1994; Tompkins and Craig 1998) while -8 K day $^{-1}$ may be more representative of the convective forcing that occurs in regions of large-scale dynamically forced ascent. This correspondence is not exact, since the moisture convergence associated with large-scale ascent is not included (see discussion by Cohen and Craig 2004). For the purposes of this paper, however, the equilibrium states are simply chosen to test of the applicability of the proposed theory over a range of forcings and cloud number densities. More particularly, since previous idealized CRM studies have shown that average cloud number is almost directly proportional to the magnitude of the large-scale forcing (Robe and Emanuel 1996; Cohen 2001), this set of simulations provide validation of the theory over a wide range of average total cloud numbers, from around 8 for the -2 K day $^{-1}$ simulation to 70 at -16 K day $^{-1}$.

In two further simulations, a mean wind shear is applied to the CRM in order to generate convective organization. A strong shear profile, identical to that of Tompkins (2000), is defined, with a surface velocity of 8 m s $^{-1}$ increasing to 12 m s $^{-1}$ at 1 km, then changing linearly to -10 m s $^{-1}$ at 12 km, and falling to 0 m s $^{-1}$ by 14.5 km. A weak shear profile is also constructed, with zero wind speed at the surface, increasing to 1 m s $^{-1}$ at 1 km, decreasing to -1 m s $^{-1}$ at 11 km, and reducing to zero at 15 km. Other model details remain the same as for the unsheared simulations. A radiative cooling rate of -8 K day $^{-1}$ is used for both these simulations, and the domain size is doubled to 256×256 km 2 , in order to generate a sufficient number of organized systems. The model is run for several days in both cases, until significant organization begins to emerge. Unlike the unsheared simulations, which were run to a complete statistically steady state, there is still a small drift in the tropospheric humidity in these runs. This should not impact the comparison with the theory for the simulated states, but it is possible that other convective regimes might emerge if the runs were extended.

3. Mass flux per cloud

The CRM is first used to verify the existence of the predicted exponential distribution of mass flux per

cloud, given in Eq. (1). Since the -2 K day $^{-1}$ simulation corresponds most closely to the low-density cloud limit required by the theory, it is chosen as the primary validation tool. However, the results for the -16 K day $^{-1}$ are also shown here for comparison.

The mass flux of each cloud within the CRM equilibrium state is diagnosed using a routine that scans through the domain and locates cloudy grid points; adjacent cloudy points are considered to be part of the same cloud and the size, σ_i , is recorded. Within each of these clouds, an average vertical velocity, \bar{w}_i , is computed and the mass flux per cloud, $m_i = \rho \sigma_i \bar{w}_i$, is calculated. Two different definitions are introduced to identify a cloudy grid point. Firstly, the standard velocity criterion, $w > 1$ ($w < -1$) m s $^{-1}$ is used to define up(down)-draft points separately (LeMone and Zipser 1980; Zipser and LeMone 1980). In the second definition, a cloudy point is identified by the presence of liquid or ice cloud water (i.e., $Q_{\text{CLD}} > 5 \times 10^{-3}$ g kg $^{-1}$). Neither of these criteria is foolproof in distinguishing between convection and other vertical motions, such as gravity waves, but as long as the results obtained using them are not too different, some degree of confidence is warranted.

Figure 1 shows the mass flux histograms from both the -2 and -16 K day $^{-1}$ simulations. The left-hand-side panels of Figs. 1a,b have been computed using the mass flux definition, $Q_{\text{CLD}} > 5 \times 10^{-3}$ g kg $^{-1}$, while the right-hand side panels are for $w > 1$ m s $^{-1}$. The $Q_{\text{CLD}} > 5 \times 10^{-3}$ g kg $^{-1}$ mass flux distribution contains a few clouds with net negative mass flux, corresponding to convective cells near the end of their life cycle, where downdraft motions dominate over the updraft component. These will be ignored in the following analysis. Conversely, in the $w > 1$ m s $^{-1}$ distributions, the weakest clouds predicted by the Boltzmann distribution will be excluded. For the relatively rare clouds with largest mass flux, the results are not likely to be statistically significant. It would be reasonable to expect the theoretical distribution to break down at some point, for example due to constraints on the dynamics of clouds whose horizontal size is larger than the depth of the troposphere, but this cannot be seen with any certainty in the figure. Nevertheless, Fig. 1 indicates that for both the -2 and -16 K day $^{-1}$ simulations, and for both mass flux definitions, the mass flux distributions appear broadly exponential, in line with theory.

A quantitative comparison with theory is provided by replotting the mass flux histograms of Fig. 1 with a logarithmic scaling of the y axes, and by fitting a linear regression through the data (Fig. 2). Taking the logarithm of Eq. (1), the slope of the regression line is equal to $\langle m \rangle^{-1}$, and thus gives an estimate of the mean mass

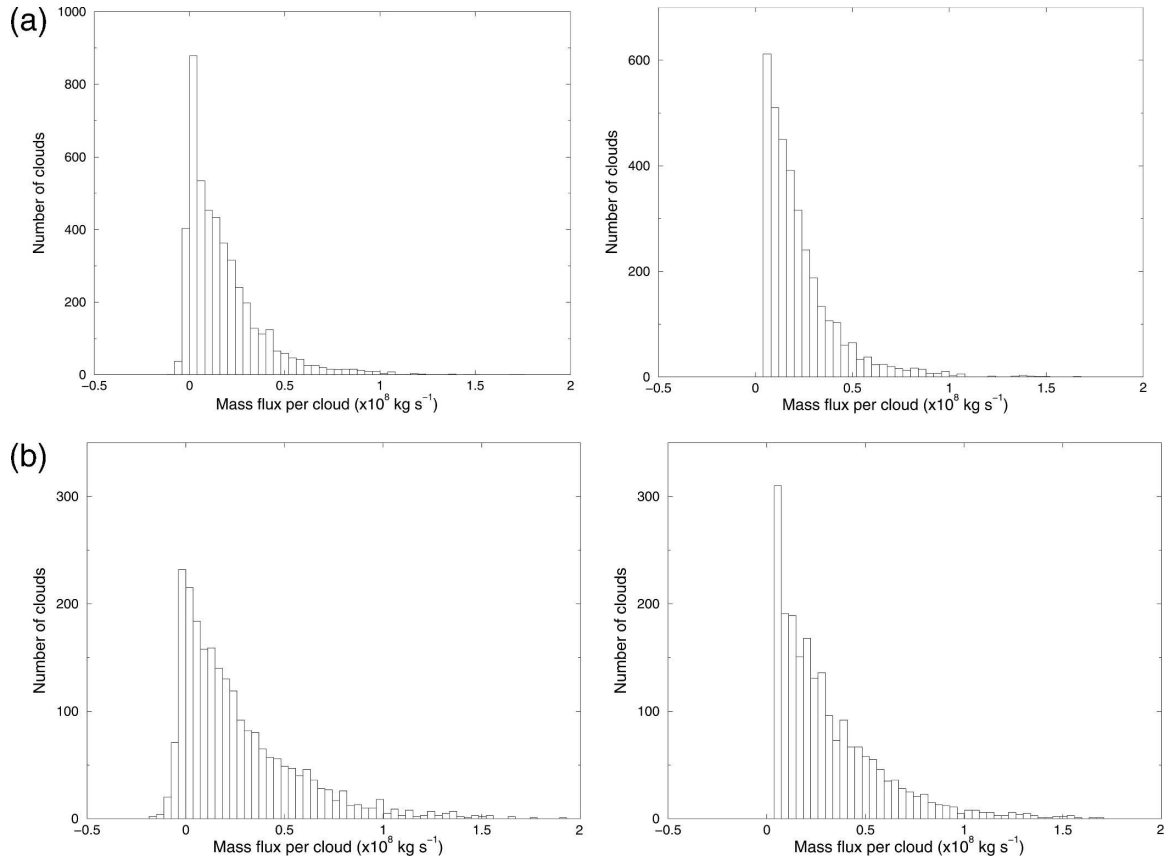


FIG. 1. Histograms of mass flux per cloud at a height of 2.4 km from the (a) -2 and (b) -16 K day^{-1} CRM simulations. (left) Mass flux criterion $Q_{\text{CLD}} > 5 \times 10^{-3} \text{ g kg}^{-1}$ and (right) $w > 1 \text{ m s}^{-1}$.

flux per cloud. The intercept is equal to $\ln(dm\langle N\rangle/\langle m\rangle)$, and gives the mean number of clouds, $\langle N\rangle$, where dm is the bin width of $2 \times 10^6 \text{ kg s}^{-1}$. Tables 1 and 2 compare the fitted values of $\langle m\rangle$ and $\langle N\rangle$ with those diagnosed from the model for both the -2 and -16 K day^{-1} simulations and, as can be seen, the agreement is very good. A similarly good agreement was found in the simulations with vertical wind shear (not shown). This suggests that, even far from the low density limit formally required by theory, cloud interactions do not play an important role in determining the distribution of cloud mass flux among individual clouds.

4. Total mass flux and variance

Time series of the total mass flux within a given region of the CRM domain can be used to test the theoretical total mass flux probability distribution of Eq. (3). Again, the -2 K day^{-1} forcing simulation is used here to provide the primary comparison with theory. Since little difference was found between the two updraft definitions, the $w > 1 \text{ m s}^{-1}$ criterion will be used henceforth.

A histogram of the total mass flux over the full model domain for the -2 K day^{-1} simulation is plotted in Fig. 3 and, as expected, shows there to be a spread of mass flux values around a well-defined mean. A curve fit of the form of Eq. (3), with free values of the parameters $\langle N\rangle$ and $\langle m\rangle$, is also plotted (solid lines), and confirms that the theoretical expression correctly predicts the shape of the simulated total mass flux distribution. A more quantitative comparison with theory, meanwhile, is provided by applying a second curve fit, with $\langle N\rangle$ and $\langle m\rangle$ now fixed to their simulated values (dashed lines). This reveals that, although overall the theoretical curve fits the CRM mass flux distribution fairly well, it predicts a mass flux variability that is larger than observed in the simulation.

The difference between the theoretical and model mass flux variance can be seen more quantitatively in Fig. 4a, where the mass flux variance for the -2 K day^{-1} simulation has been computed for a range of different sized subregions within the model domain, and is plotted directly as a function of the inverse of the average number of clouds within the region (stars). The corresponding theoretical prediction computed from Eq. (4),

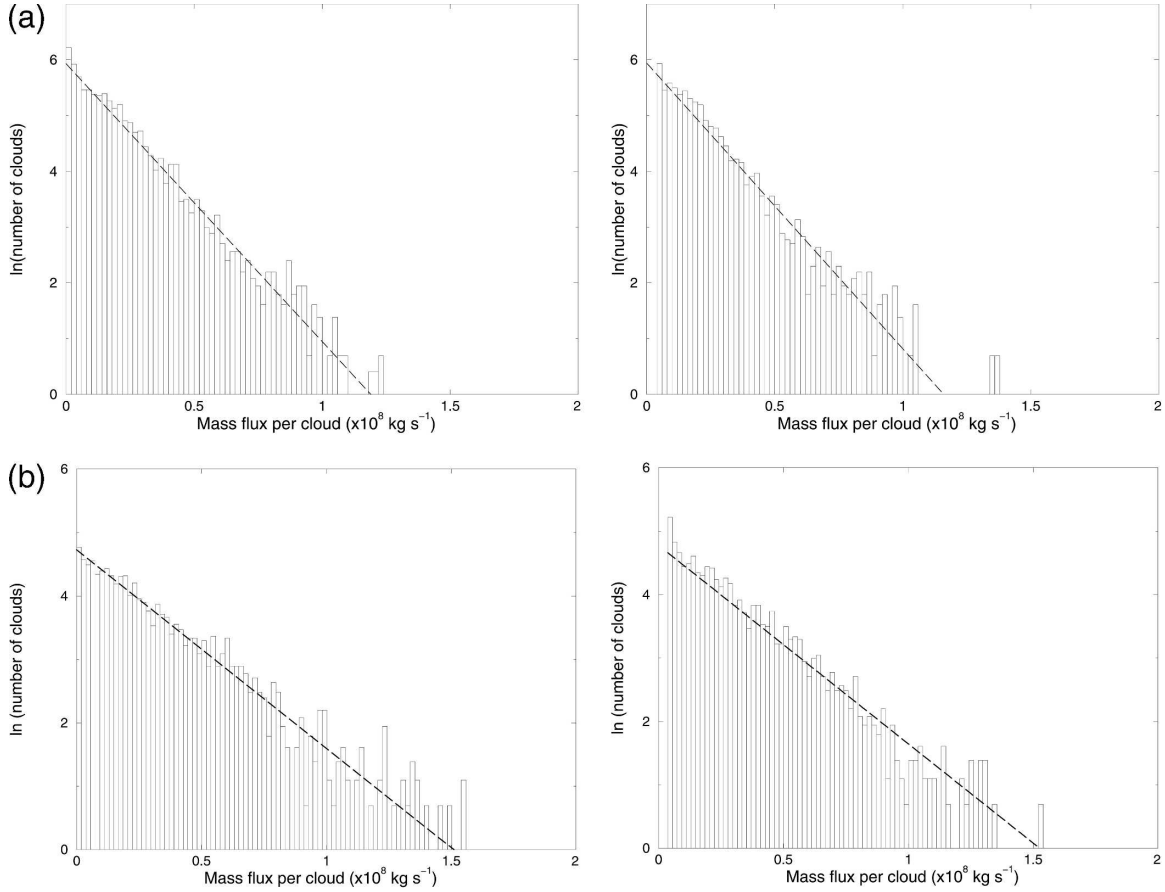


FIG. 2. As for Fig. 1, but with logarithmic scaling of the y axes. The linear regressions are also plotted (dashed lines).

a line with slope $2^{1/2}$, is also shown (dashed line). For large regions (smallest values of $1/\langle N \rangle$), the simulated variance is reasonably close to, but smaller than, the theoretical value, but appears to tail off toward smaller box sizes (the percentage error is greater than 20% for the smallest region size of $8 \times 8 \text{ km}^2$).

A possible explanation for the observed tail-off in the mass flux variance at small box sizes is that, while the theoretical argument assumes the clouds to be pointlike objects, real clouds have finite size. The starred mass flux variance points in Fig. 4a were calculated simply by summing the mass flux of all the pixels within each

given region. If a cloud straddles the boundary between two boxes, it is effectively counted as two smaller clouds (one in each box), thus increasing the mass flux variance. This effect should make little difference for a large region encompassing many clouds, but may become significant for smaller region sizes, where a greater fraction of clouds encounter a boundary. An alternative method of computing the mass flux variance, is to sum the total mass flux of each cloud whose center falls within the given region. Figure 4a (diamonds) shows that the tail-off at small region sizes is greatly reduced using this new cloud definition, and the

TABLE 1. Values of $\langle m \rangle$ and $\langle N \rangle$, diagnosed from the -2 K day^{-1} simulation of Fig. 2a, and calculated from the best-fit regression for both mass flux definitions.

Mass flux definition	$\langle m \rangle (\times 10^7 \text{ kg s}^{-1})$		$\langle N \rangle$	
	CRM	Regression	CRM	Regression
$w > 1 \text{ m s}^{-1}$	2.28	1.95	8.54	9.76
$Q_{\text{CLD}} > 5 \times 10^{-3} \text{ g kg}^{-1}$	1.95	2.01	10.44	9.89

TABLE 2. Values of $\langle m \rangle$ and $\langle N \rangle$, diagnosed from the -16 K day^{-1} simulation of Fig. 2b, and calculated from the best-fit regression for both mass flux definitions.

Mass flux definition	$\langle m \rangle (\times 10^7 \text{ kg s}^{-1})$		$\langle N \rangle$	
	CRM	Regression	CRM	Regression
$w > 1 \text{ m s}^{-1}$	3.16	3.19	68.35	67.87
$Q_{\text{CLD}} > 5 \times 10^{-3} \text{ g kg}^{-1}$	3.15	3.16	63.59	62.92

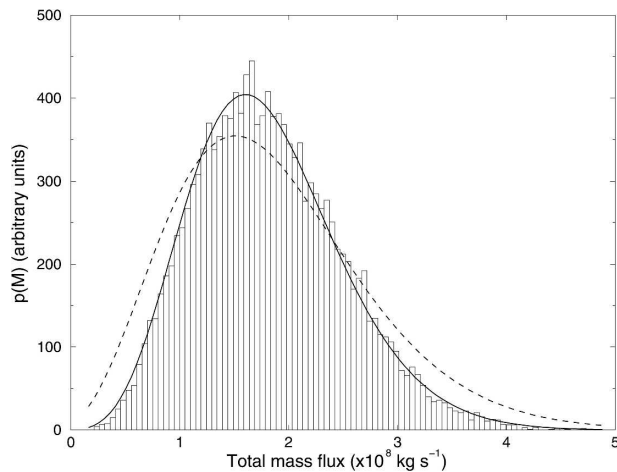


FIG. 3. Histogram of CRM total mass flux, $p(M)$, for the -2 K day^{-1} simulation. Solid line is curve-fit with parameters $\langle N \rangle$ and $\langle m \rangle$ free, dashed line is curve-fit with $\langle N \rangle$ and $\langle m \rangle$ fixed to their simulated values.

deviation between model and theory is now just over 10% for the smallest box size.

Figure 4b shows the mass flux variance as a function of region size (computed using this new cloud definition) for all five simulations (-2 , -4 , -8 , -12 , and -16 K day^{-1}), and the same relatively good fit to theory is observed at all forcings. Nevertheless, there remains a small deficit in the simulated mass flux variance that appears roughly invariant over all region sizes and over the whole forcing range. One possibility is that this discrepancy is an artifact of the finite domain size in the simulations. This effect is considered in the appendix; however, it appears that it becomes important only at the largest region sizes, and is unlikely to explain the observed variance reduction at all box sizes.

The other major assumption made in deriving the theoretical mass flux distribution was that the clouds are noninteracting, allowing their position in space to be described by a random (Poisson) distribution [Eq. (2)]. This simple model may not apply to more realistic situations such as simulated by the CRM. For example, the existence of spatial regularity within the model cloud fields would lead to a reduction in cloud number variability. This, in turn, might explain the reduction in mass flux variance observed in Fig. 4b. Spatial regularity has been seen before in both observational and modeling studies (e.g., Ramirez and Bras 1990; Ramirez et al. 1990; Nair et al. 1998), although clustering of individual cells (which would lead to increased variance) has also been reported (e.g., Randall and Huffman 1980; Sengupta et al. 1990).

The presence of clustering or regularity in the simulated cloud fields can be determined by calculating the

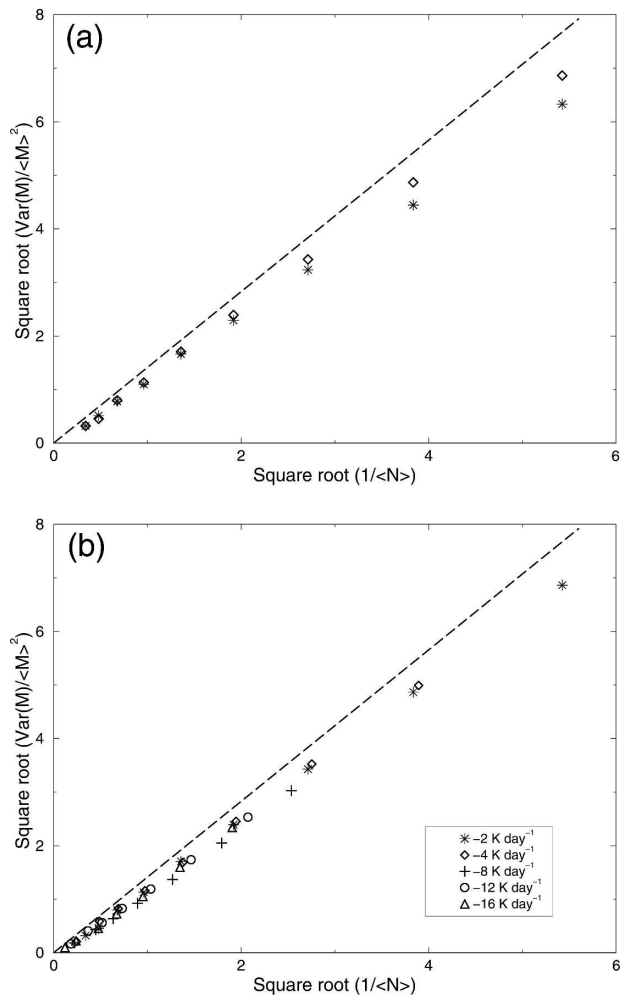


FIG. 4. Normalized total mass flux variance as a function of inverse cloud number (square rooted) for (a) -2 K day^{-1} simulation, using region definition (asterisks) and cloud definition (diamonds). (b) All forcing simulations, using cloud definition.

mean cloud number in annular regions surrounding each cloud, as a function of distance from cloud center (see the schematic in Fig. 5), and comparing the result to that expected from a random (Poisson) distribution. This statistic is similar to that used in Nair et al. (1998), although here the positioning and width of the annular regions are not rescaled by the effective mean radius of each cloud. The mean cloud number density as a function of distance from a cloud is shown in Fig. 6a for all forcing simulations. The y axis of each curve has been rescaled by the average cloud density over the whole domain. By definition, a completely random (Poisson) distribution of clouds would give a rescaled value of 1 at all distances from cloud center, and this is marked on the graph by the straight dashed line. As can be seen, the convective behavior in the vicinity of each cloud is

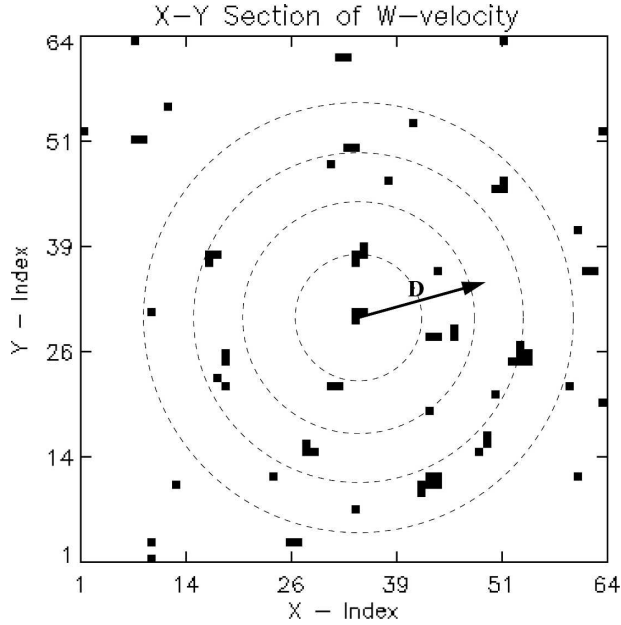


FIG. 5. Schematic of annular regions used to compute mean cloud number density as a function of radius, D , from center of a cloud.

not random, but the exact nature of these deviations varies as a function of forcing. At high forcings (-8 , -12 , and -16 K day^{-1}) there appears to be a short-range inhibition acting to reduce the density of clouds over a localized region (around 10–20 km) surrounding each cloud. This inhibition is consistent with the suggestion of spatial regularity to explain the observed reduction in mass flux variance. Figure 6a also shows a significant clustering of convective cells over the same localized range for the lowest two forcing cases (-2 and -4 K day^{-1}). This clustering would be expected to be associated with an increased mass flux variability. At distances greater than around 20 km from cloud center, these localized effects become negligible, and the mean cloud density becomes approximately random at all forcings.

To determine the magnitude of the effect of these localized cloud interactions on the cloud number variability (and perhaps on the mass flux variance), the normalized cloud number variance as a function of region size is computed for the five CRM simulations and compared to the expected Poisson values ($\equiv 1/\langle N \rangle$). For transparency, Fig. 6b shows the results only for the two extremes of the forcing range (-2 and -16 K day^{-1}); the results for the other simulations lie between these limiting cases. As can be seen, there is evidence of a slight excess in variance at -2 K day^{-1} and reduction at -16 K day^{-1} (consistent with the clustering/regularity observed in Fig. 6a), but the magnitude of the devia-

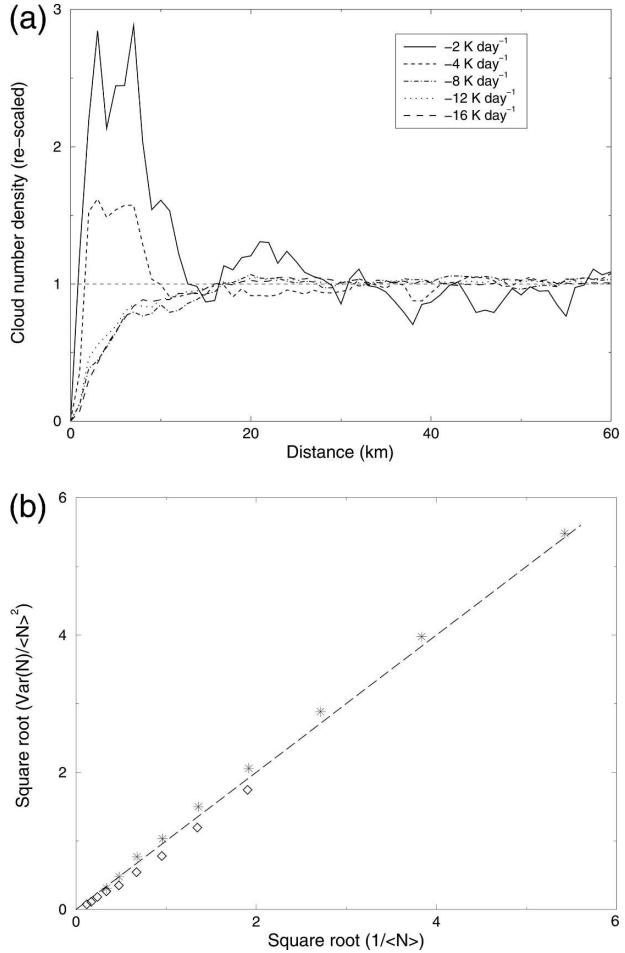


FIG. 6. (a) Rescaled cloud number density as a function of distance from cloud center for all forcing simulations. (b) Normalized cloud number variance as a function of inverse cloud number (square rooted) for the -2 (asterisks) and -16 K day^{-1} (diamonds) simulations.

tions are very small. The observed clustering or regularity in the simulations is too small to account for the reduced mass flux variance seen in Fig. 4.

One final possible cause is that there is a slight deficit in clouds with mass flux at the largest end of the exponential distribution, perhaps a result of suppression by nearby clouds. This would create a greater uniformity in the mass flux distribution than would be expected given the relatively random cloud locations, and could thus explain the reduction in the simulated mass flux variance. Because these large clouds are rare, however, it is difficult to obtain a statistically significant sample by which to test this hypothesis.

5. Organized convection

Although the statistical theory developed in Part I of this study is only strictly valid for an ensemble of non-

interacting, pointlike clouds, it has been shown to apply fairly well to CRM simulations of unorganized convection, even though localized interactions between neighboring, finite-sized clouds exist to some extent. In nature, however, cloud interactions can often become strong enough to cause organization of the individual cells into larger-scale structures, and the simple statistical theory will be less likely to apply in such situations. In this section, CRM simulations with an imposed vertical wind shear are used to investigate this issue. Horizontal cross sections of vertical velocity at 2.4 km are shown in Fig. 7, for the weak and strong shear simulations described in section 2a. The clustering of individual clouds into mesoscale arcs of convection can be seen, especially for the high shear case.

Figure 8a shows the rescaled average cloud number density as a function of distance from cloud center for both the high and low shear simulations (the curve for the -2 K day^{-1} unsheared case is also plotted for comparison) and, as expected, reveals clustering at short distances from cloud center. Interestingly, the peak of

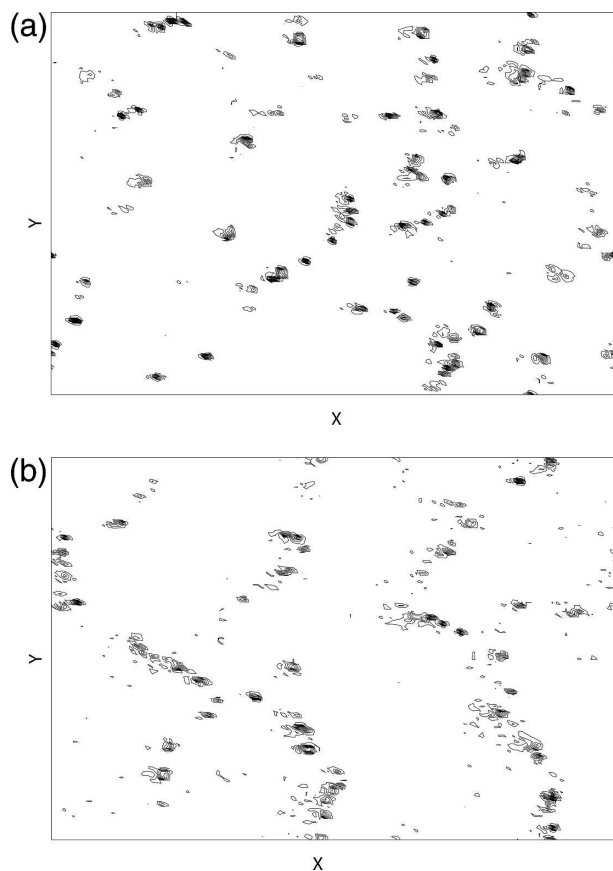


FIG. 7. Horizontal cross sections of vertical velocity at cloud-base level (2.4 km) for (a) low shear simulation and (b) high shear simulation. Both snapshots are taken several days into the run.

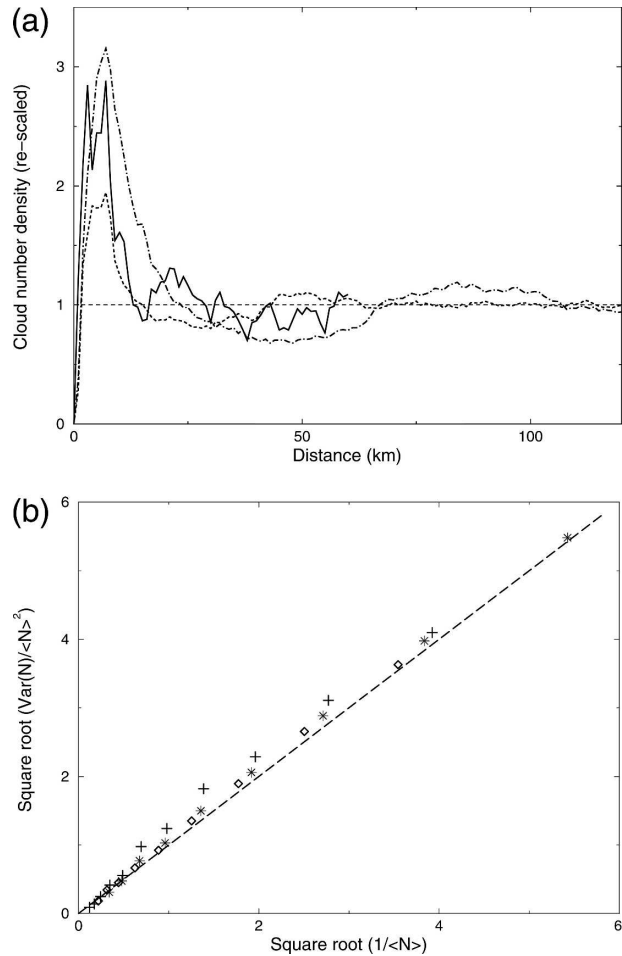


FIG. 8. (a) Rescaled cloud number density as a function of distance from cloud center for the -2 K day^{-1} (solid line), low shear (dashed), and high shear (dot-dashed) simulations. (b) Normalized cloud number variance as a function of inverse cloud number (square rooted) for the -2 K day^{-1} (asterisks), low shear (diamonds), and high shear (pluses) simulations.

this short-range clustering for both the -8 K day^{-1} , sheared simulations is similar to the -2 K day^{-1} un-sheared run, although the range of the clustering is significantly larger in the high shear case. The high shear run also seems to show an oscillation in cloud number density after the initial peak, perhaps indicating a tendency for the convection to become organized into bands separated by a constant distance (cf. Vallis et al. 1997). This same oscillation is seen to a lesser extent in the low shear simulation. The precise degree of this banding of convection, however, is difficult to infer from this plot, as a distinction between line-parallel and perpendicular directions is not made.

The convective interactions associated with the localized clustering in these sheared simulations necessarily violate the noninteracting assumption of the statistical

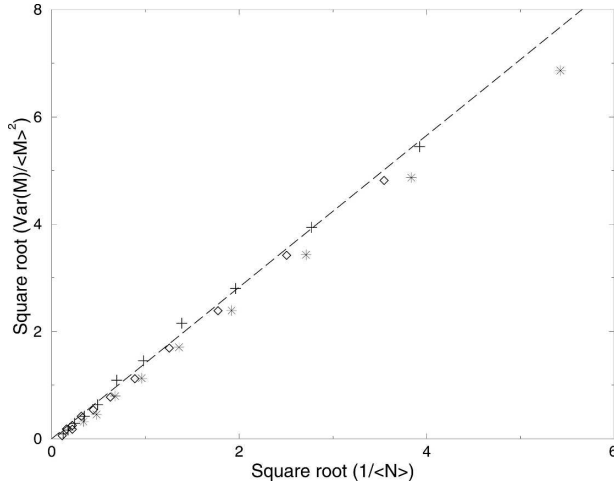


FIG. 9. Normalized total mass flux variance as a function of inverse cloud number (square rooted) for the -2 K day^{-1} (asterisks), low shear (diamonds), and high shear (pluses) simulations, using cloud definition.

theory, but it is not clear how much this will affect the cloud number and mass flux variances. Figure 8b shows the cloud number variance plot for the sheared simulations (again the -2 K day^{-1} curve is plotted for comparison). As expected, the observed convective organization is manifested as an increase in cloud number variance relative to theory, but the magnitude of these deviations from random are not large, especially for the low shear simulation. The extra variance observed in the high shear case may well be the result of the longer range of convective clustering. Although the organization of the convection is very apparent in Fig. 7, its quantitative effect on the cloud number variance is not large.

The increased cloud number variance seen in the sheared simulations would be expected to give an increase in the mass flux variance. This is plotted in Fig. 9 (with the -2 K day^{-1} unsheared curve plotted for comparison). Immediately noticeable is that the small deficit in variance observed in all the unsheared simulations (cf. Fig. 4b) has vanished for the sheared runs, and the high shear simulation even shows a slight excess of mass flux variance. This behavior is consistent with the clustering observed in the cloud number variance plot of Fig. 8b, but in fact serves mainly to offset the reduced variance seen in the unsheared simulations. Over the entire range of convective behavior explored in this study, the deviation from predictions for the highly idealized case of randomly positioned, noninteracting point clouds, is never more than about 10% of the square root variance, with the largest values found for unorganized convection over regions containing 1–10 clouds on average.

6. Conclusions and implications

In Part I of this study, a statistical theory of convective fluctuations was developed for an ensemble of noninteracting, pointlike clouds in equilibrium with the large-scale forcing. In Part II, the validity of this approach has been assessed by comparing the theoretical predictions against convective statistics from 3D cloud resolving model simulations of radiative–convective equilibrium in a nonrotating atmosphere. A relatively low fixed cooling rate of -2 K day^{-1} was chosen to correspond most closely to the low-density cloud limit required theoretically, but the validity of the theory at higher mean cloud numbers was also investigated by running additional simulations over a range of forcings from -4 to -16 K day^{-1} . The effects of convective organization were explored in two simulations with weak and strong imposed vertical wind shear.

The distribution of individual cloud mass fluxes recovered from the CRM simulations was found to be exponential at all forcings, as predicted. Summing up the mass flux from all the grid points within a given region, meanwhile, resulted in a total mass flux distribution of similar form to the predicted curve, but with slightly reduced variability. This variance deficit was shown to be worst at small box sizes. By introducing a correction to the simulated mass flux variance calculation to take account of the finite size of clouds, however, the discrepancy with theory was shown to be reduced to around 10% of the square root of variance for all region sizes and over the whole forcing range. The cause of the remaining reduction in variance was not established, although it appears that the artificial regularity associated with the finite domain size plays a role, at least for averages over regions that are close to the domain size. Simulations with imposed vertical wind shear showed organization of the convection, with significant short-range clustering in the simulated cloud fields. However, the model mass flux variance was found to be in close agreement with the theoretical prediction, with the variance increase associated with the clustering serving to approximately offset the variance reduction noted in the unsheared cases.

The implications of these results for the construction of a stochastic convective parameterization, as mooted in Part I, are that to a first approximation, the theoretical distribution can be used as is. The deviations seen here can plausibly be ignored as they are unlikely to be the greatest source of error in the resulting parameterization.

The relative unimportance of organization found here for the convective mass flux is not necessarily inconsistent with previous studies that measured organi-

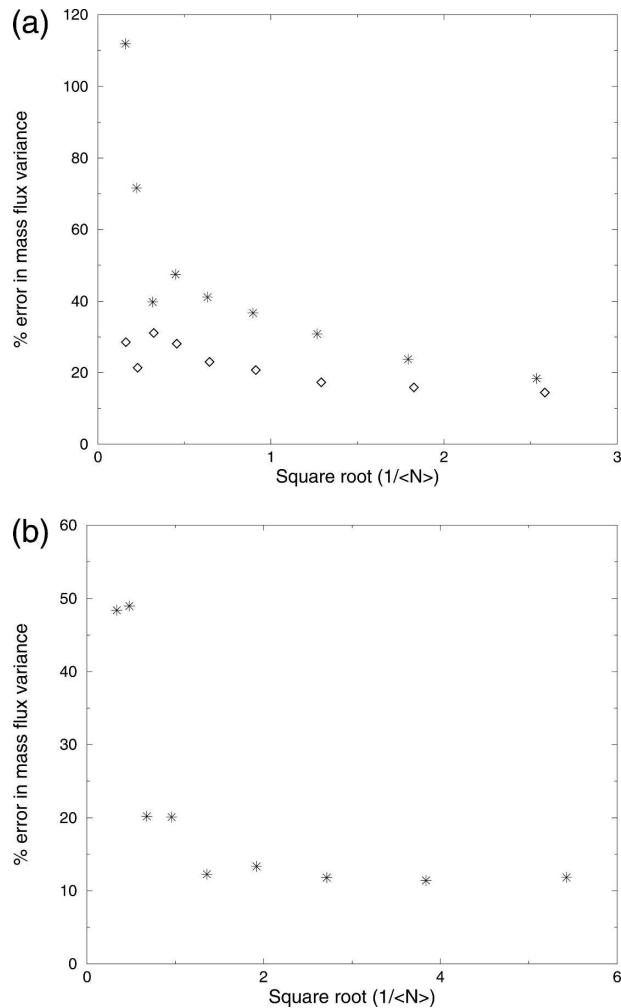


FIG. A1. Percentage error in normalized mass flux variance as a function of inverse cloud number (square rooted) for (a) -8 K day^{-1} simulation, using $128 \times 128 \text{ km}^2$ domain (asterisks) and $256 \times 256 \text{ km}^2$ domain (diamonds) and (b) -2 K day^{-1} simulation, using $128 \times 128 \text{ km}^2$ domain.

zation in cloud images, since the cloud area is governed by different processes. The long lifetime of spreading anvils can result in cloud fractions much larger than the convective fraction, and allows advective effects to become important, leading to merging of cloud regions. These effects will substantially alter the size distribution of the observed clouds, and their apparent organization. It is however a significant limitation of this study that the mass flux carried by the stratiform parts of organized convection is not treated.

APPENDIX

Finite Domain Effects on Mass Flux Variance

The magnitude of the mass flux variability obtained from the CRM simulations of this study is likely to be

affected by the finite extent of the model domain. Figure A1a shows the mass flux variance (plotted as the percentage error relative to the theoretical prediction) as a function of inverse cloud number for the -8 K day^{-1} CRM simulation on the original $128 \times 128 \text{ km}^2$ domain (stars), and also on an expanded domain of $256 \times 256 \text{ km}^2$ (diamonds). A reduction in the percentage error can be seen for the larger domain simulation, indicating that the mass flux variance is significantly altered by finite domain effects. The biggest differences between the two simulations, however, are seen for the mass flux statistics computed over large regions within the model domain (smallest values of $1/\langle N \rangle$), becoming progressively smaller as the region size decreases. Meanwhile, there remains a constant percentage error in the model variance at all region sizes, seen most clearly in Fig. A1b for the mass flux statistics from the -2 K day^{-1} simulation on the $128 \times 128 \text{ km}^2$ domain. This constant offset (of just over 10%) corresponds directly to the difference in slope observed in the mass flux variance curves of Fig. 4, and seemingly cannot be explained by the finite domain effect.

REFERENCES

- Brown, P. R. A., and H. A. Swann, 1997: Evaluation of key microphysical parameters in three-dimensional cloud-model simulations using aircraft and multiparameter radar data. *Quart. J. Roy. Meteor. Soc.*, **123**, 2245–2275.
- Cohen, B. G., 2001: Fluctuations in an ensemble of cumulus clouds. Ph.D. thesis, University of Reading, 165 pp.
- , and G. C. Craig, 2004: The response time of a convective cloud ensemble to a change in forcing. *Quart. J. Roy. Meteor. Soc.*, **130**, 933–944.
- , and —, 2006: Fluctuations in an equilibrium convective ensemble. Part I: Theoretical formulation. *J. Atmos. Sci.*, **63**, 1996–2004.
- LeMone, M. A., and E. J. Zipser, 1980: Cumulonimbus vertical velocity events in GATE. Part I: Diameter, intensity and mass flux. *J. Atmos. Sci.*, **37**, 2444–2457.
- Leonard, B. P., 1991: The ULTIMATE conservative difference scheme applied to unsteady one-dimensional advection. *Comput. Methods Appl. Mech. Eng.*, **19**, 17–74.
- MacVean, M. K., and P. J. Mason, 1990: Cloud-top entrainment instability through small-scale mixing and its parameterization in numerical models. *J. Atmos. Sci.*, **47**, 1012–1030.
- Mason, P. J., 1989: Large-eddy simulation of the convective atmospheric boundary layer. *J. Atmos. Sci.*, **46**, 1492–1516.
- Nair, U. S., R. C. Weger, K. S. Kuo, and R. M. Welch, 1998: Clustering, randomness, and regularity in cloud fields. 5. The nature of regular cumulus cloud fields. *J. Geophys. Res.*, **103**, 11 363–11 380.
- Ramirez, J. A., and R. L. Bras, 1990: Clustered or regular cumulus cloud fields: The statistical character of observed and simulated cloud fields. *J. Geophys. Res.*, **95**, 2035–2045.
- , —, and K. A. Emanuel, 1990: Stabilization functions of unforced cumulus clouds: Their nature and components. *J. Geophys. Res.*, **95**, 2047–2059.

- Randall, D. A., and G. J. Huffman, 1980: A stochastic model of cumulus clumping. *J. Atmos. Sci.*, **37**, 2068–2078.
- Robe, F. R., and K. A. Emanuel, 1996: Moist convective scaling: Some inferences from three-dimensional cloud ensemble simulations. *J. Atmos. Sci.*, **53**, 3265–3275.
- Sengupta, S. K., R. M. Welch, M. S. Navar, T. A. Berendes, and D. W. Chen, 1990: Cumulus cloud field morphology and spatial patterns derived from high spatial resolution Landsat imagery. *J. Appl. Meteor.*, **29**, 1245–1267.
- Shutts, G. J., 1991: Liquid water static energy—A moist thermodynamic variable for use in numerical models. *JCMM Mesoscale Newsletter*, No. 3, Met Office, 36–41.
- , and M. E. B. Gray, 1994: A numerical modelling study of the geostrophic adjustment process following deep convection. *Quart. J. Roy. Meteor. Soc.*, **120**, 1145–1178.
- Sui, C. H., K. M. Lau, W. K. Tao, and J. Simpson, 1994: The tropical water and energy cycles in a cumulus ensemble model. Part I: Equilibrium climate. *J. Atmos. Sci.*, **51**, 711–728.
- Swann, H., 1994: Cloud microphysical processes—A description of the parametrization used in the large eddy model. JCMM Internal Rep. 10, Met Office, 20 pp.
- Thorpe, A. J., M. J. Miller, and M. W. Moncrieff, 1982: Two-dimensional convection in non-constant shear: A model of mid-latitude squall lines. *Quart. J. Roy. Meteor. Soc.*, **108**, 739–762.
- Tompkins, A. M., 2000: The impact of dimensionality on long-term cloud-resolving model simulations. *Mon. Wea. Rev.*, **128**, 1521–1535.
- , and G. C. Craig, 1998: Radiative-convective equilibrium in a three-dimensional cloud-ensemble model. *Quart. J. Roy. Meteor. Soc.*, **124**, 2073–2097.
- Vallis, G. K., G. J. Shutts, and M. E. B. Gray, 1997: Balanced mesoscale motion and stratified turbulence forced by convection. *Quart. J. Roy. Meteor. Soc.*, **123**, 1621–1652.
- Zipser, E. J., and M. A. LeMone, 1980: Cumulonimbus vertical velocity events in GATE. Part II: Synthesis and model core structure. *J. Atmos. Sci.*, **37**, 2458–2469.